Modelization and experimental validation of CHB inverters for EVs and efficiency comparison with IGBT and SiC inverters on realistic driving cycles

Gaël Pongnot, Anatole Desreveaux, Clement Mayet, Denis Labrousse

Modelization and experimental validation of CHB inverters for EVs and efficiency comparison with IGBT and SiC inverters on realistic driving cycles

Gaël Pongnot, Anatole Desreveaux, Clément Mayet, *Member, IEEE*, Denis Labrousse

***Abstract*—Electric Vehicles (EVs) based on Cascaded H Bridge (CHB) promise reduced consumption and improved modularity, repairability, resilience, and versatility. This study focuses on evaluating the efficiency of CHB inverters utilizing low-voltage Si MOSFETs to improve EV performance and range. Through a comprehensive system-level approach and modeling, a simulation of the CHB-based powertrain is developed and experimentally validated. Electrical and mechanical simulations are conducted separately and finally combined to streamline computation times. Subsequently, CHB-based EV is compared with two-level inverters (2LI) across different driving cycles, considering multiple sources of losses from the battery to the road. Despite increased battery losses, CHB proves reduction of consumption during urban driving cycles, making it a compelling choice for sustainable commuter vehicles.**

***Index Terms*—Cascaded H-bridge (CHB), Modular multilevel converter (MMC), Multilevel inverter (MLI), Multilevel battery storage system (BSS), SiC inverter, Energetic macroscopic representation (EMR), Driving cycle, Loss evaluation, Electric Vehicles**

I. Introduction

LIMITING global warming to 1.5 °C demands rapid and deep cuts in greenhouse gas emissions [1]. Introducing carbon budgets and striving for net zero emissions are vital steps. Road transportation contributes one-sixth of global emissions [2].

Electric vehicles powered by low-GHG electricity, coupled with improved vehicle usage, could be transformative in this regard [1], [2]. In 2022, EVs accounted for 21% of European sales [3]. To penetrate the market further, EVs need better range and cost, achievable through higher battery energy density and improved drivetrain efficiency. As renewable energy sources rise, the need for energy storage grows, with EVs potentially aiding future smart grids via Vehicle-to-Grid (V2G) technology.

This work was supported by a grant overseen by the French Agency for Ecological Transition (ADEME). (corresponding author: Gaël Pongnot)

G. Pongnot is with Université Paris-Saclay, ENS Paris-Saclay, CNRS, SATIE, 91190 Gif-sur-Yvette, France (e-mail: gael.pongnot@ens-paris-saclay.fr).

A. Desreveaux and D. Labrousse are with le Conservatoire national des arts et métiers (le Cnam), 75003 Paris, France, and also with Université Paris-Saclay, ENS Paris-Saclay, CNRS, SATIE, 91190 Gif-sur-Yvette, France (e-mail: anatole.desreveaux@ens-paris-saclay.fr, denis.labrousse@ens-paris-saclay.fr).

C. Mayet is with Univ. Lille, Arts et Metiers Institute of Technology, Centrale Lille, Junia, L2EP, 59000 Lille, France (e-mail: clement.mayet@univ-lille.fr).

Manuscript received ...; revised ...

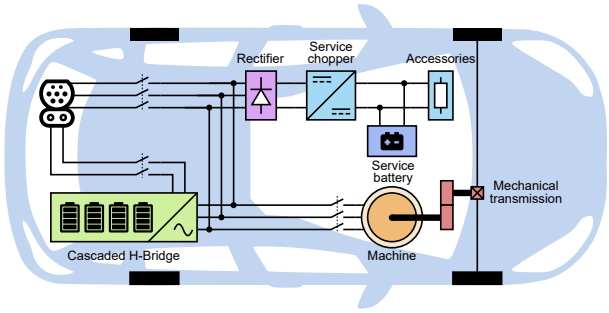

Fig. 1. Cascaded H-Bridge inverter integrated to an electric vehicle

Li-ion batteries have become essential in EVs and grid storage over the past decade [4], enabling vehicle electrification. However, their high environmental footprint, [5], poses challenges. Battery durability depends on vehicle usage [6], [7]. Addressing these issues requires improving energy and material efficiency in production and usage, enhancing system durability and resilience, and promoting circular material flows [1], [5].

Modern electric vehicles typically utilize two-level inverters (2LI), predominantly with IGBT transistors or occasionally incorporating SiC MOSFETs. The performance of this vehicle architecture is well-documented [8], [9]. However, advancements can be achieved by integrating greater intelligence into batteries [10], [11]. Various modular multilevel converter (MMC) structures, including the classical 6-legged MMC, Cascaded H-bridges (CHB), and modular multilevel series parallel (MMSP) converters, can be proposed for this purpose. However, achieving the same motor voltage with an MMC requires double the number of modules compared to a CHB, leading to complex control strategies and requiring additional inductors [12]. MMSP converters offer increased modularity through parallel battery cell association but require numerous switches, complex control strategies, and may induce cell current pulses [13], [14]. Consequently, this article focus on CHB multilevel converters, pioneered by Tolbert, Peng, and Habetler [15].

The association of CHB converters with energy storage devices has recently gained in importance [10], [16], [17]. This merging of energy storage with power electronics enables direct AC supply to the traction machine and eliminates the need for an onboard charger, figs. 1 and 2. This configuration is also investigated for grid battery storage systems (BSS) and holds promise for V2G applications [4], [18], [19].

The literature typically discusses CHB configurations with 3 to 6 modules per phase [16]–[18], [20]–[22], requiring medium-voltage Si MOSFETs, from 80 V to 120 V for 2 or 3 modules [16], [22]. In contrast, this study employs a 49-level CHB with 24 modules per phase, enabling the use of low-voltage Si MOSFETs with reduced on-resistance.

Various control strategies are available for CHB, including selective harmonic elimination (SHE) [23], [24], phase-shifted pulse width modulation (PS-PWM) [18], [20], [21], [25], and nearest level control (NLC) [17], [26]. Unlike PS-PWM, SHE and NLC exploit multiple levels to significantly reduce the switching frequency, necessitating a large number of modules to maintain waveform quality. Despite this, most articles opt for PWM techniques. In this study, with a 49-level CHB, NLC is chosen for its ease of implementation, substantial reduction in switching losses, and high waveform quality at higher voltages. However, NLC is rarely considered for power electronics losses evaluation due to the inability to create an average model.

Comparing the performance of different structures necessitates a systemic approach with equitable modeling of each element. Battery, power electronics, and machine control strategies must be collectively examined to comprehend their mutual interactions. Theliander, Kersten, Kuder, *et al.* [24] focus on battery behavior using SHE. While Chang, Ilina, Lienkamp, *et al.* [16] adopt a backward approach to compare 2LI and CHB during driving cycles, without considering battery losses. Similarly, Ali and Khalid [22] focus solely on power electronics. These works fail to account for the entirety of the powertrain, resulting in limited scopes and inevitable errors in efficiency evaluation, as they systematically neglect the interaction between batteries and electronics. Present study address this gap by comprehensively considering the various losses incurred throughout the entire powertrain, enabling a more equitable comparison with existing technologies.

To structure the system models and control of each component, Energetic Macroscopic Representation (EMR) is employed, building upon prior research [27]. EMR formalism is commonly employed in the transport field to model and control complex and multi-source energetic systems [7], [28], [29]. Its primary advantage lies in highlighting energetic interactions between subsystems while adhering to the principles of physical causality and properties [30].

Modelling cannot be used to compare structures only on result simulations for well-chosen operating points. Evaluation criteria for structures should include efficiency and consumption during constant speed sequences or realistic driving cycles [31]. However, driving cycle simulations can last several hours and require substantial computing capacities, particularly when considering electrical dynamics. Additionally, unlike PWM, NLC cannot be averaged to reduce computation time [16], [28]. Hence, our methodology distinguishes between electrical and mechanical dynamics to address these challenges.

Therefore, the key contribution of this article is to compare CHB, IGBT and SiC inverters demonstrating the need for system approach. The following sections are organized as follows. Firstly, section 2 presents CHB inverter structure and its model. Our developed simulation tools are validated by comparison with real tests on CHB prototype. Then, section 3 shows a comparison with conventional 2LI structures, IGBT and SiC, from the model to the efficiency in the torque-speed field. Finally, section 4 focus on the usage of these structures for an electric vehicle, combining them with a vehicle model including mechanical simulations. Evaluation and conclusion are made on consumption during driving cycles.

II. Cascaded H-Bridge inverter

A. Structure and operating mode

A Cascaded H-bridge inverter supplies the electric machine with three phases p, fig. 2. Three legs, each consisting of M serial modules (24 in this case), produce the phase voltages v_p. A module comprises the association of an N-cell battery (4 in this instance) with an H-bridge. The switches are created using low voltage MOSFETs. To avoid on-board charger and achieve European electric grid compatibility (230-400 V), the embedded battery cells must be increased, totaling 288 cells.

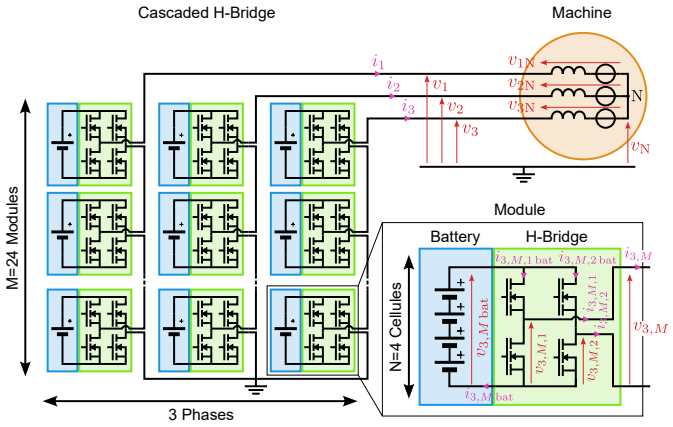

Fig. 2. Cascaded H-Bridge inverter connected to a Y-configured machine

The phase voltages v_p can be expressed as the sum of module voltages $v_{p,m}$, eq. (1). Each module carry the same phase current, eq. (2). By construction, eqs. (3) and (4) demonstrate couplings inside a module from the machine side, while eqs. (5) and (6) show the same from the battery side.

$$v_p = \sum_{m=1}^{M} v_{p,m} \tag{1}$$

$$i_{p,m} = i_p \tag{2}$$

$$v_{p,m} = v_{p,m,1} - v_{p,m,2} \tag{3}$$

$$i_{p,m,1} = -i_{p,m,2} = i_{p,m} \tag{4}$$

$$v_{p,m,b\,\mathrm{bat}} = v_{p,m\,\mathrm{bat}} \tag{5}$$

$$i_{p,m\,\mathrm{bat}} = i_{p,m,1\,\mathrm{bat}} + i_{p,m,2\,\mathrm{bat}} \tag{6}$$

The Nearest Level Command (NLC) is employed, leveraging the multitude of available levels. This strategy selects the nearest available level from the reference, chosen for its

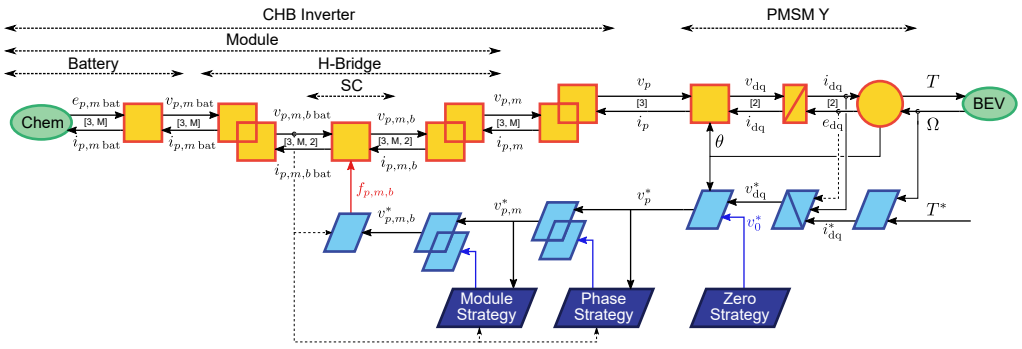

Fig. 3. Energetic Macroscopic Representation of a CHB Inverter with a Y-PMSM

simplicity and reduced switching count compared to other waveform modulations. On average, each transistor switch less than twice during an electric period, making this choice pertinent given the large number of modules considered.

B. Modelling

This paper adopts the Energetic Macroscopic Representation (EMR) formalism to organize and interconnect models based on physical energy properties. EMR, derived from Bond Graph theory, provides a graphical depiction of complex systems, illustrating interactions between elements through action-reaction links while maintaining physical causality [30]. This technique effectively highlights the energetic properties of the system, enabling the deduction of control structures and strategies through model inversion [26].

The EMR of a CHB inverter connected to a machine is depicted in Figure 3, providing the foundation for the ensuing model equations. Vector representation is employed for a concise and adaptable model, with vector dimensions indicated between arrows. Equations (1) to (6) are represented using coupling elements : double orange squares.

1) Batteries: Lithium batteries are intricate electrochemical systems that can be accurately modeled, but their complexity makes them impractical for implementation in powertrain simulations. The dynamic behavior of batteries is generally modelled with a serial RC network and a static resistor. These models provides a reasonably accurate description of cell behavior.

In most vehicular studies, only the static resistor is considered in the models because, in the case of a 2-Level Inverter (2LI), the battery current remains constant when the output power is constant. However, Theliander, Kersten, Kuder, *et al.* [24] demonstrated that considering dynamic behavior leads to improved efficiency in the case of CHB inverters, due to the low-frequency component of the current. Despite this, for the sake of reducing simulation times, this article intentionally overestimates losses by employing a static model, see eq. (7).

$$v_{p,m\,\mathrm{bat}} = \underbrace{N\,e_{\mathrm{cell}}}_{e_{\mathrm{bat}}} - \underbrace{N\,R_{\mathrm{cell}}}_{R_{\mathrm{bat}}}\,i_{p,m\,\mathrm{bat}} \tag{7}$$

Balancing module state of charge (SoC) is addressed by various strategies developed for each control technique: SHE [23], PS-PWM [18], [20], [21], and NLC [17], [26]. All these strategies have demonstrated the capability to balance the SoC effectively. Hence, this paper assumes that the battery cells are perfectly balanced, and the open circuit voltage (OCV) e_{cell} is identical for every cell.

2) Si MOSFET: The H-bridge legs are controlled by a switching command $f_{p,m,b}$ for switching cells (SC), illustrated in fig. 3, with b representing the bridge index (1 or 2). These legs experience both conduction and switching losses. Conduction losses are modeled using a voltage drop attributed to a series resistance $R_{\mathrm{DS_{on}}}$, see eq. (8). Additionally, switching losses are modeled by an additional input current $i_{p,m,b\,\mathrm{sw}}$, see eq. (9).

$$v_{p,m,b} = f_{p,m,b}\,v_{p,m,b\,\mathrm{bat}} - R_{\mathrm{DS_{on}}}\,i_{p,m,b} \tag{8}$$

$$i_{p,m,b\,\mathrm{bat}} = f_{p,m,b}\,i_{p,m,b} + i_{p,m,b\,\mathrm{sw}} \tag{9}$$

Incorporating switching losses for Si MOSFETs is challenging because unlike IGBT or SiC modules, manufacturers do not typically provide a characteristic of dissipated energies. While analytical models do exist, they often require numerous parameters and may lack fair accuracy [32].

In this study, switching energies will be determined using simplified formulas, see eq. (10), following previous approaches [16], [33], which are based on an Infineon application note. Three distinct terms are considered: channel conduction E_{mos}, diode recovery E_{rec}, and diode conduction during freewheel time E_{fw}. Their calculation relies on : the switching time t_{sw}, the free-wheel time t_{fw}, the reverse recovery charge Q_{rr} and the diode model V_F and R_D.

$$\begin{cases} E_{\mathrm{mos}} = v_{p,m,b\,\mathrm{bat}}\,i_{p,m,b}\,t_{\mathrm{sw}}/2 \\ E_{\mathrm{rec}} = Q_{\mathrm{rr}}\,v_{p,m,b\,\mathrm{bat}} \\ E_{\mathrm{fw}} = (V_{\mathrm{F}} + R_{\mathrm{D}}\,i_{p,m,b})\;i_{p,m,b}\,t_{\mathrm{fw}} \end{cases} \tag{10}$$

The energies calculated as described are utilized as an additional input current pulse on the battery side, as shown in eq. (11), during a simulation period T_{sim} and when switching is detected, denoted as $\delta_{sw} = 1$.

$$i_{p,m,b\,\mathrm{sw}} = \frac{E_{\mathrm{mos}} + E_{\mathrm{rec}} + E_{\mathrm{fw}}}{T_{\mathrm{sim}}\,v_{p,m,b\,\mathrm{bat}}}\delta_{\mathrm{sw}} \tag{11}$$

3) Permanent magnet synchronous machine (PMSM): A synchronous machine with permanent magnets and salient poles is considered. The machine's behavior in the Park domain is described by Equations (12) to (16). Dynamic effects are derived from the inductances L_d and L_q. According to the following equations, the PMSM presented in Figure 3 comprises three elements: Park transform, inductive energy storage, and magneto-mechanical conversion.

$$\begin{cases} L_\mathrm{d}(i_\mathrm{d}, i_\mathrm{q})\, i_\mathrm{d} = \int (v_\mathrm{d} - e_\mathrm{d} - R_\mathrm{Cu}(\omega)\, i_\mathrm{d})\, \mathrm{d}t \\ L_\mathrm{q}(i_\mathrm{d}, i_\mathrm{q})\, i_\mathrm{q} = \int (v_\mathrm{q} - e_\mathrm{q} - R_\mathrm{Cu}(\omega)\, i_\mathrm{q})\, \mathrm{d}t \end{cases} \tag{12}$$

Copper losses are represented by a resistor in series with the windings $R_\mathrm{Cu}(\omega)$. This resistance includes a DC component, which represents DC current losses, and a quadratic component dependent on the speed ω, indicative of the skin effect in the conductors. It is incorporated in the equation for inductances, eq. (12), depicted in figs. 3 and 8 by the energy storage element.

$$\begin{cases} e_\mathrm{d} = -\omega\, \Phi_\mathrm{q}(i_\mathrm{d}, i_\mathrm{q}) \\ e_\mathrm{q} = +\omega\, \Phi_\mathrm{d}(i_\mathrm{d}, i_\mathrm{q}) \end{cases} \tag{13}$$

Magnetic fluxes Φ_d and Φ_q are functions of currents i_d and i_q. These flows are used in the expressions for electromotive forces (emf) e_d and e_q, eq. (13), as well as the electromagnetic torque T_em, eq. (14). These equations takes place on fig. 3 into the multi-physical conversion element.

$$T_\mathrm{em} = n_\mathrm{p}\, (\Phi_\mathrm{d}(i_\mathrm{d}, i_\mathrm{q})\, i_\mathrm{q} - \Phi_\mathrm{q}(i_\mathrm{d}, i_\mathrm{q})\, i_\mathrm{d}) \tag{14}$$

$$\omega = n_\mathrm{p} \Omega \tag{15}$$

Iron losses are considered through a resistive torque T_Fe calculated for a torque-speed operating point, as shown in Equation 16. This element is highly dependent on the control law employed, so they must be determined together.

$$T = T_\mathrm{em} - T_\mathrm{Fe}(\Omega, T_\mathrm{em}) \tag{16}$$

4) Control and energy management: The system operates in torque control mode, with the BEV source effectively acting as an infinite inertia that dictates the machine's rotational speed. The magneto-mechanical element is inverted using predetermined machine maps aimed at minimizing current amplitude, referred to as Maximum Torque per Ampere (MTPA), which generate reference currents i_d^* and i_q^* based on reference torque T^* and measured speed Ω [34], [35]. The machine inductances inversion requires a current controller, implemented with a Proportional-Integral (PI) controller to generate target dq voltages. Prior to performing the inverse Park transform, a zero strategy may be introduced to modulate the neutral point potential.

After finalizing machine control, the CHB inverter must provide the requisite phase voltages v_p^*. Transitioning from 3 pieces of information to $3M$, the inversion of series module coupling, eqs. (1) and (2), allows for enhanced degrees of freedom. These are used to balanced the SoC among the various battery modules [26]. Additionally, as described in eq. (3), each H-bridge has four available configurations for only three output states. The selection between the two zero-voltage configurations is governed by the Module Strategy block, which alternates between them. Finally, NLC is operated to recreate the sinusoids and determine the $6M$ command orders $f_{p,m,b}$.

As EMR is a flexible organisation tool, offering a quick and simple means to modify the configuration of complex systems by highlighting the coupling between different subsystems. This approach facilitates adjustments to the number of modules M and the quantity of battery cells per module N. Employing multiple strategy blocks within the proposed framework simplifies the implementation of various control strategies, such as alternative balancing methods or different modulation techniques. Ultimately, adopting the approach outlined in this paper enables the consideration of diverse losses and constraints for each subsystem. Consequently, it becomes feasible to separately quantify the contribution of each subsystem, as demonstrated in this study.

C. Simulation of operating points

The simulation is conducted based on the previously expressed models to analyze the waveforms and energetic quantities at each operating point (OP). Figure 4 illustrates two critical OPs: high speed and high torque, both representing the same mechanical power of 30 kW.

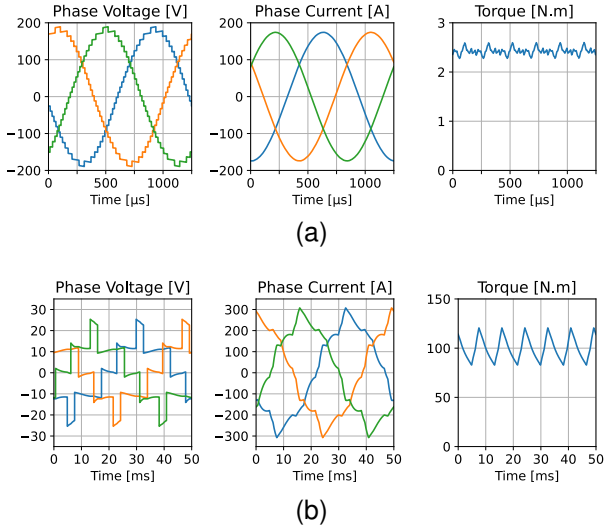

Fig. 4. Scopes of critical operating points. (a) High speed and low torque (12 000 rpm, 2.5 N m). (b) High torque and low speed (300 rpm, 100 N m)

Impact of NLC is readily observed on these figures : voltages progress in steps resembling stairs to form the desired sinusoidal waveform. The current produced by the structure at fig. 4a closely resembles a perfect sinusoid. Conversely, when lower voltage levels are utilized, as shown in fig. 4b, fewer modules are activated, resulting in a degradation of the current waveform quality in the machine and consequently leading to torque ripple. Furthermore, high currents affect the voltage waveform, causing fluctuations in the voltage steps due to voltage drops induced by phase currents.

D. Experimental validation

A real size static prototype have been developed with a battery capacity of 30 kWh [36] and a total of 72 modules, fig. 5. Figure 6 illustrates a real operating point of the CHB inverter connected to a driving machine. The voltage waveform exhibits distinct steps, indicating a poor low-frequency harmonic content. However, the current remains smooth, with only minor variations between pole pairs due to mechanical imperfections in the machine.

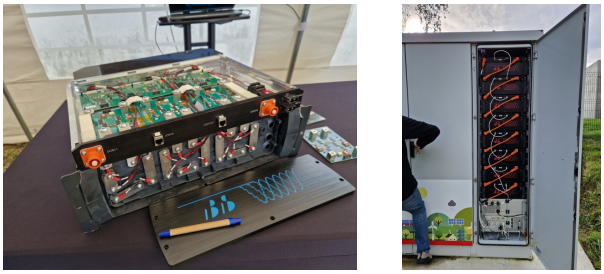

Fig. 5. Photos of a 49-level CHB prototype [36]. (a) Cluster of 3 modules. (b) Phase rack.

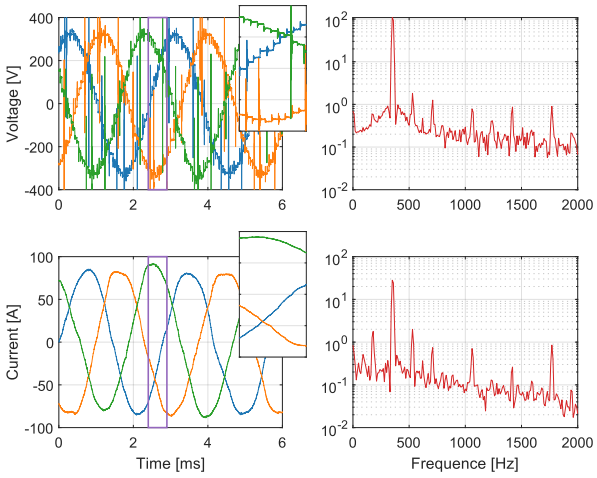

Fig. 6. Experimental waveform at 5200 rpm and 40 N m

The primary objective of this article is to examine efficiency and consumption. Therefore, the validation of the simulated model will focus on energetic quantities. To achieve this, the efficiency of the CHB inverter (comprising power electronics and battery) is evaluated for three operating points through both experimental tests and simulations, as shown in table I.

The measurement tests are conducted during a discharge and recharge cycle of the battery. Initially, the State of Charge (SoC) is set to 90 %, and the battery is discharged to a SoC of 30 % using the driving machine at the selected operating point. The energy flowing from the structure to the machine is measured using an integrator power meter. Subsequently, the battery is charged using AC recharge mode with a known efficiency until reaching 90 % SoC again. The operating point efficiency is then deduced by considering the discharge and recharge energies, along with the recharge efficiency. A wide range of SoC variation enhances the precision of SoC estimation at start and end points but directly impacts efficiency due to the OCV variation, resulting in a mean value.

However, the duration of the tests directly depends on the power of the operating point and the battery capacity. The tests conducted in this study required up to 6 hours for each, and lower power tests would necessitate even more time, potentially spanning days. Therefore, the validation is limited to three medium-power points.

TABLE I
VALIDATION OF EFFICIENCY ESTIMATION

Speed [rpm]	2000	3500	5200
Torque [N.m]	60	50	40
Experiment [%]	90.7	95.4	96.1
Simulation [%]	92.6	94.9	96.2

Table I demonstrates promising findings, with experimental results closely matching simulations, differing by less than two percentage points, thus validating the previous models.

III. Comparison with two-level inverters (2LI)

A. Structure and operating mode

A two-level inverter (2LI) acts as an interface between a high-voltage DC bus and a 3-phase traction machine, utilizing six high-voltage, high-current switches, typically IGBTs or SiC MOSFETs, along with diodes.

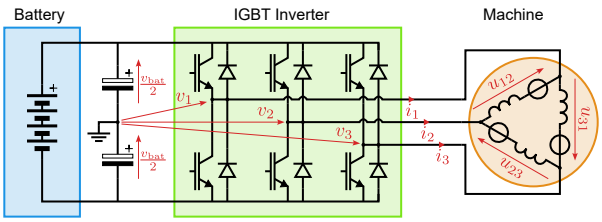

Fig. 7. Two-level inverter connected to a Δ-configured machine

When employing SiC MOSFETs, the DC bus voltage commonly increases, for instance, from 400 V to 800 V [37]. This DC bus is supplied by a battery pack, which consists of battery cells arranged in series or parallel connections. To create a 400-volt DC bus, two parallel branches of 108 serial Li-ion NMC cells are used. When operating a 2LI, the available output voltage is directly proportional to the DC bus voltage and the number of serially connected cells S.

In the following, the SiC 2LI is used with a 800-volts DC bus at a switching frequency of 20 kHz, double of the IGBT 2LI in both cases [37]. To ensure a fair comparison of the impact on power electronics and the battery, the same machine is utilized in both cases. For consistency, the machine is configured as Δ for the IGBT setup and as Y for the SiC configuration. This configuration ensures that the available voltages observed by the machine are similar, table II.

The CHB configuration embed an increased number of cells compared to 2LI configurations, due to the AC grid connection

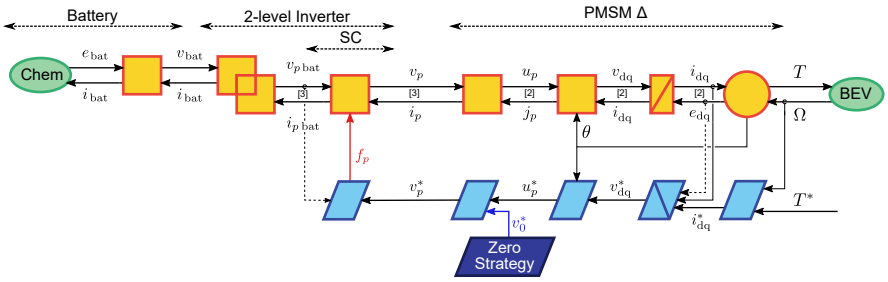

Fig. 8. Energetic Macroscopic Representation of a 2L-Inverter with a Δ-PMSM

TABLE II
AVAILABLE VOLTAGE AND PMSM CONFIGURATION

	2L Inverter		CHB Inverter
Battery pack	108S2P	216S1P	24M4N
DC bus	400 V	800 V	-
Phase voltage	$\sqrt{2}/4\ SV_{\text{cell}}$		$\sqrt{2}/2\ MNV_{\text{cell}}$
	140 V	**280 V**	**250 V**
Line voltage	**245 V**	490 V	430 V
PMSM config.	Δ	Y	Y

constraint outlined in section II-A. This adjustment results in the phase and line voltages presented in table II. To ensure a fair comparison, the CHB will be Y-configured similar to the SiC MOSFET 2LI, while the IGBT 2LI will be Δ-configured.

B. Modelling of IGBT and SiC inverters

Two-level inverters require a constant direct current from the battery when the output power remains constant, which is the case in electric simulations aiming to determine static operating points. Therefore, this article employs only a classical serial resistor model, as depicted in eq. (17). Dynamic behaviors are thus disregarded, like in most 2LI studies, having no effect on losses and efficiency assessments.

The serial resistance R_{bat} and open-circuit voltage e_{bat} of the batteries are influenced by the characteristics of individual cells, denoted by e_{cell} and R_{cell}, as well as the configuration of the battery pack. In this study, a serial-parallel battery pack is analyzed, comprising S serial cells and P parallel branches.

$$v_{\text{bat}} = \underbrace{S\, e_{\text{cell}}}_{e_{\text{bat}}} - \underbrace{\frac{S}{P} R_{\text{cell}}}_{R_{\text{bat}}}\ i_{\text{bat}} \tag{17}$$

A DC bus connects the battery to the inverter legs (SC). The coupling element on Figure 8 (double orange square) represents this parallel association described by Equations (18) and (19).

$$\forall p,\ \ v_{p\,\text{bat}} = v_{\text{bat}} \tag{18}$$

$$i_{\text{bat}} = \sum_{p=1}^{3} i_{p\,\text{bat}} \tag{19}$$

Inverter legs are managed by a switching command f_p, experiencing conduction and switching losses. Conduction losses are represented by a voltage drop $v_{p\,\text{cd}}$, eq. (20), while switching losses are captured by an additional input current $i_{p\,\text{sw}}$, eq. (21).

$$v_p = f_p v_{\text{bat}} - v_{p\,\text{cd}} \tag{20}$$

$$i_{p\,\text{bat}} = f_p i_p + i_{p\,\text{sw}} \tag{21}$$

For IGBTs, the voltage drop $v_{p\,\text{cd}}$ is contingent on the command f_p and the current i_p, as shown in eq. (22). To estimate component voltages v_{F} and v_{CE}, a diode model is applied, eq. (23), which is also suitable for IGBTs. Similarly, for SiC MOSFETs, the voltage drop is directly proportional to the forward current, as depicted in eq. (24), akin to Si MOSFETs.

$$v_{p\,\text{cd}} = \begin{cases} f_p\, v_{\text{CE}}(i_p) + (f_p - 1)\, v_{\text{F}}(i_p) & \text{if } i_p \geq 0 \\ f_p\, v_{\text{F}}(-i_p) + (f_p - 1)\, v_{\text{CE}}(-i_p) & \text{else if } i_p \leq 0 \end{cases} \tag{22}$$

$$v(i) = V_{\text{th}} \log\left(1 + \frac{i}{I_{\text{sat}}}\right) + R\, i \tag{23}$$

$$v_{p\,\text{cd}} = R_{\text{DS}_{\text{on}}} i_p \tag{24}$$

Switching losses are determined by the product of the frequency and the switching energy. The latter is typically provided by manufacturers under specific conditions and can be fitted using linear or quadratic models depending on the bus voltage v_{bat} and phase current i_p. Reference values for the considered IGBT and SiC modules are outlined in Table III. These losses are integrated into the model, as shown in eq. (25), by adding an additional input current $i_{p\,\text{sw}}$, defined as the switching losses FE_{sw} divided by the battery voltage v_{bat}.

$$i_{p\,\text{sw}} = \frac{E_{\text{sw}}}{v_{\text{bat}}} F \tag{25}$$

When the switching frequency is significantly higher than the desired signal frequency, the command signal f_p can be replaced by its average value during a switching period α. Equations (20) to (22) remain valid in this scenario, and simulation steps can be wider than the switching period.

TABLE III
TRANSISTORS REFERENCES

Transistor	Reference	Producer	Volt. rat.
IGBT	FS400R07A1E3	Infineon	650 V
MOSFET Si	confidential	-	< 80 V
MOSFET SiC	ADP280120W3	STMicro	1200 V

C. Efficiency in Torque-Speed field

Simulations of the efficiency across a wide range of OPs are depicted in Figure 9, illustrating efficiency maps in the Torque-Speed field for various structures: IGBT 2LI, SiC 2LI, and CHB. These maps consider efficiency across batteries, power electronics, and the machine.

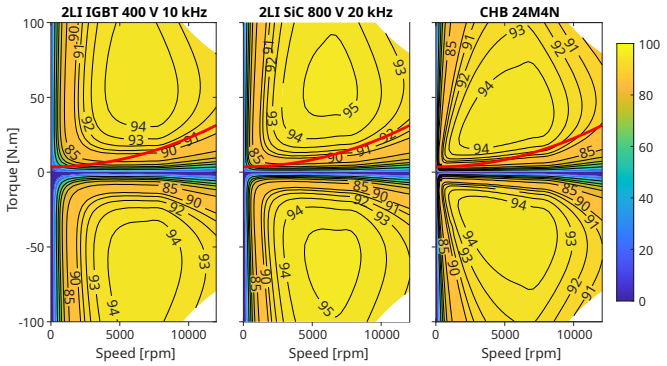

Fig. 9. Efficiency maps of the IGBT and SiC 2LI, and CHB powertrains. The red curve represents the constant speed torque of the vehicle.

Figure 9 illustrates that the highest efficiency is attained with SiC MOSFET 2LI, reaching 95.3 %. IGBT 2LI shows a slower efficiency growth at low speeds, whereas SiC 2LI and CHB exhibit enhancements in this aspect. Hence, an enhancement in vehicle efficiency during urban cycles can be expected.

Regenerative braking stands as one of the most significant improvements in electric vehicles compared to internal combustion engine counterparts. Nevertheless, its indiscriminate use can lead to inefficiencies, with certain areas of the Torque-Speed field resulting in zero efficiency at low speed, wherein battery energy is consumed for braking purposes. Hence, the implementation of braking strategies becomes imperative in vehicles [38]. As illustrated in Figure 9, these inefficient regions are considerably smaller for SiC 2LI compared to IGBT 2LI, and even smaller for CHB configurations.

Finally, vehicles are predominantly operated at low power levels, which plays to the advantage of CHB configurations since their higher-efficiency regions typically align with lower power outputs compared to 2LI setups.

IV. Electric Vehicle and Realistic Conditions

A. Methodology

Simulating a driving cycle (20 minutes) with a simulation step compatible with electric period representation (8 ms at 100 km/h) can be computationally expensive. While estimating the energetic behavior of a PWM-driven system is sufficient with an average model [16], [28], the Nearest Level Control strategy involves few switchings, sometimes using only a few voltage levels. Therefore, simulations should deliver accurate waveforms to ensure precise estimations of switching losses.

To avoid costly computation times, simulations are divided between electrical and mechanical ones, which is possible because mechanical dynamics are significantly slower than electrical ones. This process is illustrated in Figure 10: a first simulation campaign is conducted from the battery to the

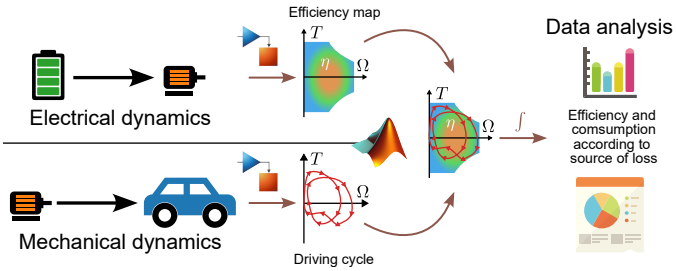

Fig. 10. Methodology, separated electrical and mechanical simulation

machine to obtain efficiency maps in the torque-speed field, followed by a second campaign from the machine output to the road to generate driving cycle trajectories in the same field. The resulting data are then merged to determine the efficiency and consumption of each element in the traction chain for driving cycles. This approach gives similar results as an unique simulation while reducing the computational burdens.

B. Mechanical transmission and vehicle models

A simplified longitudinal model of the BEV is employed, assuming straight motion without considering curves. Consequently, the torques of both sides wheels are assumed to be perfectly equal. These hypotheses result in the EMR depicted in fig. 11. Three energy sources are represented: the electric drive (ED), the mechanical brake, and the environment.

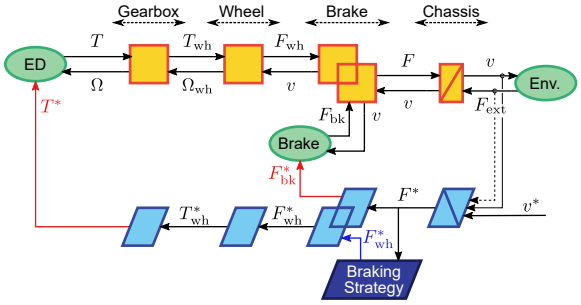

Fig. 11. EMR of an electric vehicle

TABLE IV
Vehicle Parameters

	Symbol	Value
Vehicle mass	m	1600 kg
Dynamic mass	m_{dyn}	1635 kg
Gearbox ratio	r_{gb}	9.8
Wheel radius	R_{wh}	350 mm
Drag coefficient	SC_{x}	0.645 m^2
Rolling resistance	C_{rr}	6.2×10^{-3}
Air density	ρ	1.2 kg/m^3

The gearbox and differential are characterized by eq. (26), where T represents the mechanical torque for the PMSM and Ω denotes its rotational speed. The reduction ratio r and other vehicle parameters are specified in Table IV. A constant efficiency η_{gb} is assumed and applied depending on power flow sign. These equations correspond to the relevant conversion element depicted in fig. 11.

$$\begin{cases} T_{\mathrm{wh}} = r\,T\,\eta_{\mathrm{gb}}^{\mathrm{sign}(\Omega T)} \\ \Omega = r\,\Omega_{\mathrm{wh}} \end{cases} \tag{26}$$

Under the assumption of straight motion, a single equivalent wheel is represented by eq. (27). The wheel radius R_{wh} converts rotation to linear motion, where T_{wh} denotes the torque applied to the equivalent wheel, and Ω_{wh} represents its rotational speed.

$$\begin{cases} F_{\mathrm{wh}} = T_{\mathrm{wh}}/R_{\mathrm{wh}} \\ \Omega_{\mathrm{wh}} = v/R_{\mathrm{wh}} \end{cases} \tag{27}$$

An EMR source represent the mechanical brake, which imposes a braking force F_{bk} equal to its reference F_{bk}^{*}, determined by the control of the BEV. The braking force F_{bk} and force from the wheel F_{wh} are summed in eq. (28) to create the driving force F of the vehicle. During slowdown phases, a braking strategy needs to choose a distribution between regenerative and dissipative brake according to the ED limits. various solutions are available, as described by [39], [40].

$$F = F_{\mathrm{wh}} + F_{\mathrm{bk}} \tag{28}$$

The vehicle's motion is influenced by its dynamic mass m_{dyn}, composed of its mass m and the inertia of its rotating parts, eq. (29). The vehicle speed v is determined by Newton's Law, eq. (30), calculated as the integral of the difference between the total traction/braking force F and the resisting force of the environment F_{ext}. The latter, given by eq. (31), accounts for rolling and drag forces.

$$m_{\mathrm{dyn}} = m + \frac{4J_{\mathrm{wh}} + J_{\mathrm{gb}}}{R_{\mathrm{wh}}^2} \tag{29}$$

$$v = \frac{1}{m_{\mathrm{dyn}}} \int (F - F_{\mathrm{ext}})\,\mathrm{d}t \tag{30}$$

$$F_{\mathrm{ext}} = C_{\mathrm{rr}} mg + \frac{1}{2}\rho S C_{\mathrm{x}} v^2 \tag{31}$$

C. Constant speed study

Given the vehicle model, the torque required to sustain a constant speed is computed eq. (32), and depicted in red on fig. 9. The efficiency corresponding to this red curve is determined on fig. 12. Moreover, the consumption C attributable to the traction chain can be evaluated using eq. (33) as the expended energy E divided by the distance d (driving cycle) or the expended power P divided by the vehicle speed v.

$$T = \frac{R_{\mathrm{wh}}}{\eta_{\mathrm{gb}}\, r}\left(C_{\mathrm{rr}} mg + \frac{1}{2}\rho S C_{\mathrm{x}}\left(\frac{R_{\mathrm{wh}}}{r}\Omega\right)^2\right) \tag{32}$$

$$C = \frac{E}{d} = \frac{P}{v} \tag{33}$$

The plots depicted in Figure 12 illustrate superior efficiency and lower consumption for CHB in comparison to SiC and IGBT 2LI at low speeds. While SiC demonstrates better performance than IGBT in this setup, CHB nearly reaches the minimum achievable consumption owing to the machine's performance constraints and despite using Nearest Level Control. The lowest consumption for each structure varies with speed and is less (both in speed and consumption) for CHB compared to SiC and IGBT, as outlined in table V.

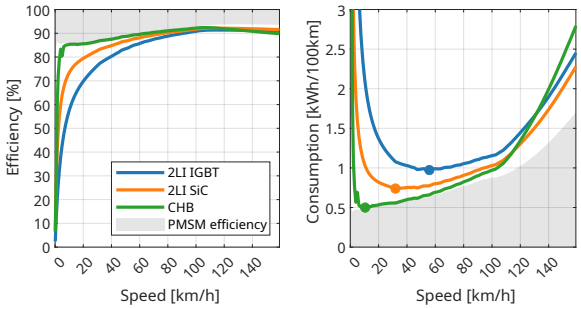

Fig. 12. Efficiency and consumption of the traction chain at constant speed

TABLE V
LOWEST CONSTANT SPEED CONSUMPTION FROM BATTERY TO MACHINE

	CHB	2LI SiC	2LI IGBT
Speed [km/h]	10.5	31.9	55.8
Consumption [kWh/100km]	0.50	0.74	0.97

On the contrary, CHB exhibits the highest consumption at high speeds exceeding 130 km/h, performing worse than IGBT. Nonetheless, this observation needs to be contextualized within the influence of mechanical transmission and aerodynamic forces, which predominantly affect consumption at high speeds. Beyond 40 km/h, the powertrain contributes to less than 20% of the vehicle's consumption, a proportion that diminishes towards 10% at higher speeds.

By nature, the constant speed approach neglects vehicle dynamics and only examines a limited portion of the torque-speed field. However, in reality, a significant portion of a vehicle's energy consumption occurs during dynamic phases. Thus, driving cycles are essential for a more comprehensive evaluation.

D. Driving cycle analysis

To evaluate and compare vehicule's consumptions in realistic conditions, several driving cycles have been developped: WLTC, USA City, Artemis... Here, INRETS cycles will be used as they are representative of diverse European driving scenarios, encompassing slow urban traffic (UL1), smooth urban traffic (UF1), road (R1), highway (A1) conditions [31].

Figure 13 illustrates the exploration of the torque-speed field by each of speed profile. As expected, urban driving cycles predominantly operate at low speeds, while road and highway profiles venture into higher speeds. Additionally, road and highway cycles exhibit greater torque utilization for more significant accelerations. Notably, the A1 cycle mainly operates at high speeds and low torque, indicating constant high-speed driving.

The vehicle's comsumption can be split into four terms: three for the powertrain (battery, power electronics and machine) and one for the rest (mechanical transmission, rolling

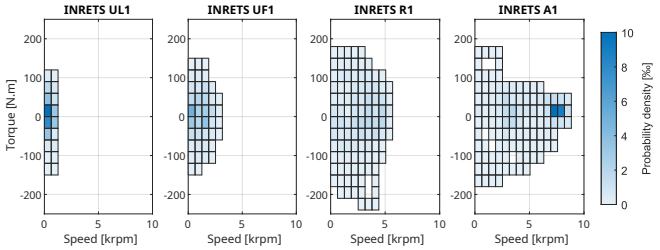

Fig. 13. Torque-Speed histogram of four driving cycles

White to blue scale : occurrence frequency on arbitrary scale

and aerodynamic resistance) grouped under "rolling" term. The machine and rolling consumptions are independent of the converter structure and remain consistent across different structures for the same driving cycle.

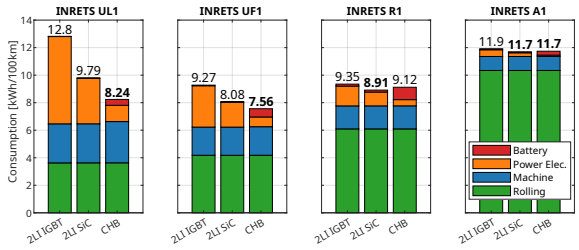

Fig. 14. Consumption of the EV for four driving cycles

Figure 14 shows the simulated consumption of each element for the considered cycles. The use of CHB inverter allows a great reduction of the consumption in slow urban speed profile (UL1) compared to IGBT and SiC. CHB losses are no longer located in power electronics but also in batteries. High speed driving cycle illustrates the little impact of power electronics and battery on the consumption. In this configuration, no significant gains are expected from replacing the 2LI architecture.

V. Conclusion

A comparative study of power converters structure for EV based on SiC MOSFET 2LI, IGBT 2LI, and Cascaded H-Bridge (CHB) inverters reveals that SiC MOSFET 2LI achieves the highest efficiency in the torque-speed domain, reaching 95.3 %. Moreover, IGBT 2LI exhibits limited efficiency at low speeds, while SiC 2LI and CHB show significant improvements, suggesting a potential increase in the efficiency of electric vehicles during urban driving cycles.

An analysis of efficiency maps, constant-speed curves, and driving cycles reveals that the CHB exhibits superior efficiency and lower consumption at low speeds compared to SiC and IGBT 2LI. However, at very high speeds, CHB shows higher consumption than SiC 2LI, although this is mitigated by the dominant influence of mechanical transmissions and aerodynamic forces at these speeds. Implementing a CHB inverter leads to a significant reduction in consumption during urban cycles compared to IGBT and SiC options. Nonetheless, a limitation remains in maintaining the same vehicle mass regardless of the structure.

Despite CHB-based EV offering improved efficiencies, our findings suggest an increase in battery losses. This, combined with changes in current loads, could potentially affect the lifespan of battery cells. Further investigation is required.

The CHB-based EV model and its control, presented in this paper, establish a versatile simulation tool that integrates all constraints and strategies of the real system, including losses. This tool has been validated through comparison with the real system. Moreover, this method facilitates the adjustment of system parameters and the implementation of various control strategies. Moving forward, future studies will focus on optimizing the distribution of cells within the structure to determine the optimal division (M, N) of the battery into modules. Altering the cell distribution affects the waveform, and its implications on machine performance, as well as harmonic content during recharge, will need to be evaluated.

The control strategy used here (NLC) has the advantage of requiring very little switching. Contrary to initial expectations in the literature regarding its performance at low speeds, our findings suggest that NLC can be an efficient choice when a sufficient number of levels are available. Exploring alternative strategies like pulse width modulation may improve waveform quality. A comparative study on the impact of these strategies on efficiency, cell and machine aging, and harmonic distortion could provide valuable insights.

CHB-based EVs seem to have a bright future. The reduction in consumption is obvious. Combining these benefits with the structure's advantages in terms of modularity, repairability, resilience, and versatility makes it a key asset for future EVs.

Acknowledgement

This document results of the IBIS research project funded by ADEME under the French Government's "Programme d'investissements d'avenir (PIA)."

References

[1] K. Calvin, D. Dasgupta, G. Krinner, *et al.*, "IPCC, 2023: Climate Change 2023: Synthesis Report. Contribution of Working Groups I, II and III to the Sixth Assessment Report of the Intergovernmental Panel on Climate Change [Core Writing Team, H. Lee and J. Romero (eds.)]," Intergovernmental Panel on Climate Change (IPCC), Geneva, Switzerland, Tech. Rep., Jul. 2023, pp. 1–34. DOI: 10.59327/IPCC/AR6-9789291691647.

[2] L. Paoli, A. Dasgupta, and S. McBain, "Electric Vehicles," IEA, Paris, Tech. Rep., 2022.

[3] IEA, *Global EV Outlook 2023 : Trends in electric light-duty vehicles*, https://www.iea.org/energy-system/transport/electric-vehicles, Apr. 2023.

[4] F. Eroğlu, M. Kurtoğlu, and A. M. Vural, "Bidirectional DC–DC converter based multilevel battery storage systems for electric vehicle and large-scale grid applications: A critical review considering different topologies, state-of-charge balancing and future trends," *IET Renewable Power Generation*, vol. 15, no. 5, pp. 915–938, 2021, ISSN: 1752-1424. DOI: 10.1049/rpg2.12042.

[5] X. Lai, Q. Chen, X. Tang, *et al.*, "Critical review of life cycle assessment of lithium-ion batteries for electric vehicles: A lifespan perspective," *eTransportation*, vol. 12, p. 100 169, May 2022, ISSN: 2590-1168. DOI: 10.1016/j.etran.2022.100169.

[6] M. Jafari, A. Gauchia, S. Zhao, K. Zhang, and L. Gauchia, "Electric Vehicle Battery Cycle Aging Evaluation in Real-World Daily Driving and Vehicle-to-Grid Services," *IEEE Transactions on Transportation Electrification*, vol. 4, no. 1, pp. 122–134, Mar. 2018, ISSN: 2332-7782. DOI: 10.1109/TTE.2017.2764320.

[7] A. Ndiaye, R. German, A. Bouscayrol, *et al.*, "Impact of the User Charging Practice on the Battery Aging in an Electric Vehicle," *IEEE Transactions on Vehicular Technology*, pp. 1–10, 2024, ISSN: 1939-9359. DOI: 10.1109/TVT.2024.3356116.

[8] N. Wassiliadis, M. Steinsträter, M. Schreiber, *et al.*, "Quantifying the state of the art of electric powertrains in battery electric vehicles: Range, efficiency, and lifetime from component to system level of the Volkswagen ID.3," *eTransportation*, vol. 12, p. 100 167, May 2022, ISSN: 2590-1168. DOI: 10.1016/j.etran.2022.100167.

[9] D.-D. Tran, M. Vafaeipour, M. El Baghdadi, *et al.*, "Thorough state-of-the-art analysis of electric and hybrid vehicle powertrains: Topologies and integrated energy management strategies," *Renewable and Sustainable Energy Reviews*, vol. 119, p. 109 596, Mar. 2020, ISSN: 1364-0321. DOI: 10.1016/j.rser.2019.109596.

[10] L. Komsiyska, T. Buchberger, S. Diehl, *et al.*, "Critical Review of Intelligent Battery Systems: Challenges, Implementation, and Potential for Electric Vehicles," *Energies*, vol. 14, no. 18, p. 5989, Jan. 2021, ISSN: 1996-1073. DOI: 10.3390/en14185989.

[11] Z. Zhao, H. Hu, Z. He, *et al.*, "Power Electronics-Based Safety Enhancement Technologies for Lithium-Ion Batteries: An Overview From Battery Management Perspective," *IEEE Transactions on Power Electronics*, vol. 38, no. 7, pp. 8922–8955, Jul. 2023, ISSN: 1941-0107. DOI: 10.1109/TPEL.2023.3265278.

[12] M. Quraan, T. Yeo, and P. Tricoli, "Design and Control of Modular Multilevel Converters for Battery Electric Vehicles," *IEEE Transactions on Power Electronics*, vol. 31, no. 1, pp. 507–517, Jan. 2016, ISSN: 1941-0107. DOI: 10.1109/TPEL.2015.2408435.

[13] N. Sorokina, J. Estaller, A. Kersten, *et al.*, "Inverter and Battery Drive Cycle Efficiency Comparisons of Multilevel and Two-Level Traction Inverters for Battery Electric Vehicles," in *2021 IEEE International Conference on Environment and Electrical Engineering and 2021 IEEE Industrial and Commercial Power Systems Europe (EEEIC / I&CPS Europe)*, Sep. 2021, pp. 1–8. DOI: 10.1109/EEEIC/ICPSEurope51590.2021.9584705.

[14] F. Helling, J. Glück, A. Singer, H.-J. Pfisterer, and T. Weyh, "The AC battery – A novel approach for integrating batteries into AC systems," *International Journal of Electrical Power & Energy Systems*, vol. 104, pp. 150–158, Jan. 2019, ISSN: 01420615. DOI: 10.1016/j.ijepes.2018.06.047.

[15] L. Tolbert, F. Z. Peng, and T. Habetler, "Multilevel converters for large electric drives," *IEEE Transactions on Industry Applications*, vol. 35, no. 1, pp. 36–44, Jan. 1999, ISSN: 1939-9367. DOI: 10.1109/28.740843.

[16] F. Chang, O. Ilina, M. Lienkamp, and L. Voss, "Improving the Overall Efficiency of Automotive Inverters Using a Multilevel Converter Composed of Low Voltage Si mosfets," *IEEE Transactions on Power Electronics*, vol. 34, no. 4, pp. 3586–3602, Apr. 2019, ISSN: 1941-0107. DOI: 10.1109/TPEL.2018.2854756.

[17] L. Mathe, P. Dan Burlacu, E. Schaltz, and R. Teodorescu, "Battery pack state of charge balancing algorithm for cascaded H-Bridge multilevel converters," in *2016 IEEE 16th International Conference on Environment and Electrical Engineering (EEEIC)*, Jun. 2016, pp. 1–6. DOI: 10.1109/EEEIC.2016.7555737.

[18] L. Maharjan, S. Inoue, H. Akagi, and J. Asakura, "State-of-Charge (SOC)-Balancing Control of a Battery Energy Storage System Based on a Cascade PWM Converter," *IEEE Transactions on Power Electronics*, vol. 24, no. 6, pp. 1628–1636, Jun. 2009, ISSN: 1941-0107. DOI: 10.1109/TPEL.2009.2014868.

[19] J. Fang, F. Blaabjerg, S. Liu, and S. M. Goetz, "A Review of Multilevel Converters With Parallel Connectivity," *IEEE Transactions on Power Electronics*, vol. 36, no. 11, pp. 12 468–12 489, Nov. 2021, ISSN: 1941-0107. DOI: 10.1109/TPEL.2021.3075211.

[20] F. Eroglu, M. Kurtoglu, A. Eren, and A. M. Vural, "A novel adaptive state-of-charge balancing control scheme for cascaded H-bridge multilevel converter based battery storage systems," *ISA Transactions*, Oct. 2022, ISSN: 0019-0578. DOI: 10.1016/j.isatra.2022.09.044.

[21] M. Vasiladiotis and A. Rufer, "Balancing control actions for cascaded H-bridge converters with integrated battery energy storage," in *2013 15th European Conference on Power Electronics and Applications (EPE)*, Sep. 2013, pp. 1–10. DOI: 10.1109/EPE.2013.6634337.

[22] A. Ali and H. A. Khalid, "Comparative Analysis of Two-Level and Multilevel CHB Topologies for EV Drivetrain," in *2023 International Conference on Emerging Power Technologies (ICEPT)*, May 2023, pp. 1–6. DOI: 10.1109/ICEPT58859.2023.10152403.

[23] L. Tolbert, F. Z. Peng, T. Cunnyngham, and J. Chiasson, "Charge balance control schemes for cascade multilevel converter in hybrid electric vehicles," *IEEE Transactions on Industrial Electronics*, vol. 49, no. 5, pp. 1058–1064, Oct. 2002, ISSN: 1557-9948. DOI: 10.1109/TIE.2002.803213.

[24] O. Theliander, A. Kersten, M. Kuder, *et al.*, "Battery Modeling and Parameter Extraction for Drive Cycle Loss Evaluation of a Modular Battery System for Vehicles Based on a Cascaded H-Bridge Multilevel Inverter," *IEEE Transactions on Industry Applications*, vol. 56, no. 6, pp. 6968–6977, Nov. 2020, ISSN: 1939-9367. DOI: 10.1109/TIA.2020.3026662.

[25] B. McGrath and D. Holmes, "Multicarrier PWM strategies for multilevel inverters," *IEEE Transactions on Industrial Electronics*, vol. 49, no. 4, pp. 858–867, Aug. 2002, ISSN: 1557-9948. DOI: 10.1109/TIE.2002.801073.

[26] C. Mayet, D. Labrousse, R. Bkekri, F. Roy, and G. Pongnot, "Energetic Macroscopic Representation and Inversion-Based Control of a Multi-Level Inverter with Integrated Battery for Electric Vehicles," in *2021 IEEE Vehicle Power and Propulsion Conference (VPPC)*, Gijon, Spain: IEEE, Oct. 2021, pp. 1–6. DOI: 10.1109/VPPC53923.2021.9699228.

[27] G. Pongnot, C. Mayet, and D. Labrousse, "Loss Distribution in an Electric Vehicle Traction Chain using a Cascaded H-Bridge Inverter with Integrated Battery," in *PCIM Europe 2023*, Nuremberg, Germany, May 2023, pp. 1–7. DOI: 10.30420/566091062.

[28] A. Desreveaux, E. Labouré, O. Bethoux, *et al.*, "Fast Computational Dynamic Model of Traction Drive for Electric Vehicles," in *2022 IEEE Vehicle Power and Propulsion Conference (VPPC)*, Nov. 2022, pp. 1–6. DOI: 10.1109/VPPC55846.2022.10003383.

[29] P. Arboleya, C. Mayet, B. Mohamed, J. A. Aguado, and S. de la Torre, "A review of railway feeding infrastructures: Mathematical models for planning and operation," *eTransportation*, vol. 5, p. 100 063, Aug. 2020, ISSN: 2590-1168. DOI: 10.1016/j.etran.2020.100063.

[30] A. Bouscayrol and B. Lemaire-Semail, "Energetic macroscopic representation and inversion-based control," in *Encyclopedia of Electrical and Electronic Power Engineering*, J. García, Ed., Oxford: Elsevier, Jan. 2023, pp. 365–375, ISBN: 978-0-12-823211-8. DOI: 10.1016/B978-0-12-821204-2.00117-3.

[31] M. André, "The ARTEMIS European driving cycles for measuring car pollutant emissions," *Science of The Total Environment*, Highway and Urban Pollution, vol. 334–335, pp. 73–84, Dec. 2004, ISSN: 0048-9697. DOI: 10.1016/j.scitotenv.2004.04.070.

[32] D. Christen and J. Biela, "Analytical Switching Loss Modeling Based on Datasheet Parameters for mosfets in a Half-Bridge," *IEEE Transactions on Power Electronics*, vol. 34, no. 4, pp. 3700–3710, Apr. 2019, ISSN: 1941-0107. DOI: 10.1109/TPEL.2018.2851068.

[33] D. D. Graovac, M. Pürschel, and A. Kiep, *MOSFET Power Losses Calculation Using the Datasheet Parameters*, Jun. 2006.

[34] S. Morimoto, Y. Tong, Y. Takeda, and T. Hirasa, "Loss minimization control of permanent magnet synchronous motor drives," *IEEE Transactions on Industrial Electronics*, vol. 41, no. 5, pp. 511–517, Oct. 1994, ISSN: 1557-9948. DOI: 10.1109/41.315269.

[35] R. Ni, D. Xu, G. Wang, *et al.*, "Maximum Efficiency Per Ampere Control of Permanent-Magnet Synchronous Machines," *IEEE Transactions on Industrial Electronics*, vol. 62, no. 4, pp. 2135–2143, Apr. 2015, ISSN: 1557-9948. DOI: 10.1109/TIE.2014.2354238.

[36] J.-C. Lefebvre and V. Gillot, *IBIS: Stellantis and Saft Reveal a Smarter, More Efficient Battery for Autos and Stationary Power*, https://www.stellantis.com/en/news/press-releases/2023/july/ibis-stellantis-and-saft-reveal-a-smarter-more-efficient-battery-for-autos-and-stationary-power, Jul. 2023.

[37] I. Aghabali, J. Bauman, P. J. Kollmeyer, *et al.*, "800-V Electric Vehicle Powertrains: Review and Analysis of Benefits, Challenges, and Future Trends," *IEEE Transactions on Transportation Electrification*, vol. 7, no. 3, pp. 927–948, Sep. 2021, ISSN: 2332-7782. DOI: 10.1109/TTE.2020.3044938.

[38] F. Naseri, E. Farjah, and T. Ghanbari, "An Efficient Regenerative Braking System Based on Battery/Supercapacitor for Electric, Hybrid, and Plug-In Hybrid Electric Vehicles With BLDC Motor," *IEEE Transactions on Vehicular Technology*, vol. 66, no. 5, pp. 3724–3738, May 2017, ISSN: 1939-9359. DOI: 10.1109/TVT.2016.2611655.

[39] A. S. Murthy, D. P. Magee, and D. G. Taylor, "Vehicle braking strategies based on regenerative braking boundaries of electric machines," in *2015 IEEE Transportation Electrification Conference and Expo (ITEC)*, Jun. 2015, pp. 1–6. DOI: 10.1109/ITEC.2015.7165809.

[40] G. Pongnot, C. Mayet, and D. Labrousse, "Comparison of Different Braking Strategies to Improve the Energy Recovery of an Electric Vehicle Based on Cascaded H-Bridge Inverter with Batteries," in *2023 IEEE Vehicle Power and Propulsion Conference (VPPC)*, Milano, Italia, Oct. 2023, pp. 1–6. DOI: 10.1109/VPPC60535.2023.10403284.